Volume 18
Number 11
19 March 2026
Pages 5607-6124

Nanoscale

rsc.li/nanoscale

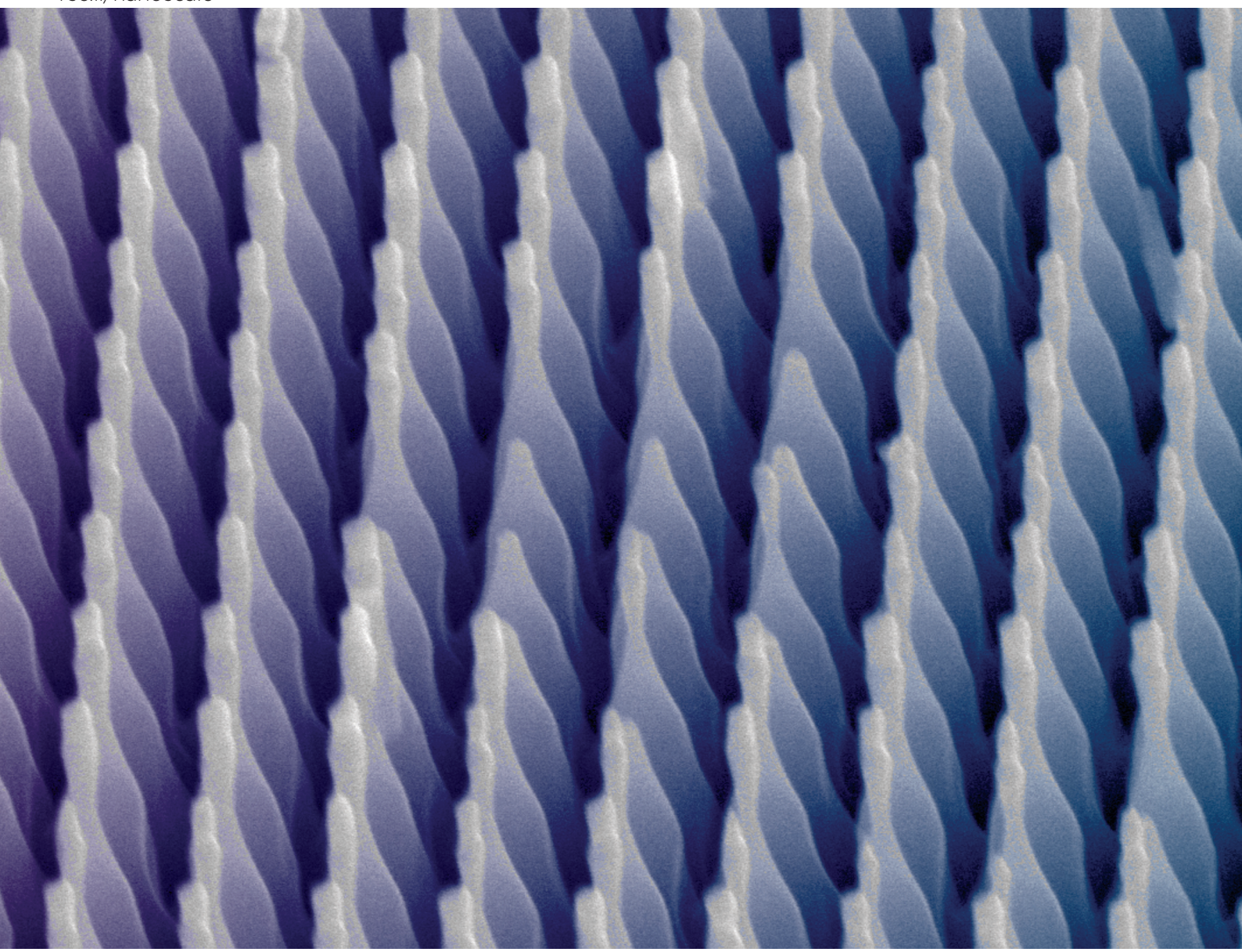

ISSN 2040-3372

ROYAL SOCIETY OF CHEMISTRY

PAPER
Chih-Hao Chang *et al.*
From resilience to scratch resistance: engineering the deformation mechanisms of nanostructured surfaces

NCNST

Nanoscale

PAPER

View Article Online
View Journal | View Issue

Cite this: *Nanoscale*, 2026, **18**, 5769

From resilience to scratch resistance: engineering the deformation mechanisms of nanostructured surfaces

Mehmet Kepenekci, Kun-Chieh Chien, Natalia A. Rueda Guerrero, Kwon Sang Lee and Chih-Hao Chang *

Received 11th December 2025,
Accepted 13th February 2026

DOI: 10.1039/d5nr05216e

rsc.li/nanoscale

Nanostructured materials and engineered surfaces have attracted significant attention for their unique physical properties in multiple domains. The structural geometry and material composition have a profound influence on the mechanical behavior of these structures but have yet to be systematically examined. This work investigates the effect of the pillar aspect ratio and intrinsic material properties on the deformation mechanisms of sapphire and silicon nanopillar arrays. Using nanoindentation, the modulus, hardness, and scratch resistance of silicon and sapphire nanopillar arrays with various aspect ratios are characterized. The results indicate that low aspect ratio nanopillar arrays have high hardness and stiffness but are brittle and fail through material fracture. On the other hand, high aspect ratio nanopillars are more resilient and exhibit recoverable deformation through structure buckling and bending. The sapphire nanopillar arrays are more mechanically robust compared to silicon and have modulus and hardness comparable to bulk glass and other scratch-resistant metals. The findings guide the development of mechanically robust nanostructured materials with optimized surface properties and can find applications in nanophotonics, multifunctional surfaces, and nanoscale devices.

I. Introduction

Many insects, plants, and animals employ nanostructures with novel material properties to increase their chance of surviving and creating offspring. Examples include the tapered subwavelength nanostructures on the eyes of moths (*Attacus atlas*), which emulate a gradient-index medium to suppress Fresnel reflection losses.[1,2] Another nanostructure in biology is the surface roughness of the lotus (*Nelumbo nucifera*) leaf, which enables the composite Cassie–Baxter wetting state to create the water-repelling and self-cleaning properties of plant surfaces.[3,4] Researchers have been examining these structures to understand the underlying mechanisms to inspire the engineering of nanostructured materials with enhanced optical and wetting properties. These biomimetic materials are used in a wide range of applications in anti-fouling, drag reduction, displays, photonics, and renewable energy.[5–9]

The geometry of the nanostructures plays a key role in the operating mechanisms and the resulting physical properties. One of the key parameters is the ratio of the feature height (h) to width (w), defined as the aspect ratio (AR), where AR = h/w. For optimal antireflection behavior, tall and dense nanostructures are needed to enhance response at long and short wavelengths, respectively.[10,11] Recent work on silicon antireflection structures with high AR demonstrated solar panel efficiency enhancement by decreasing the reflectivity and improving the omnidirectional absorption.[12] Similarly, high AR and dense nanostructures improve the pressure robustness of the Cassie–Baxter state, enhancing the self-cleaning effect for dynamic droplet impact or hydrostatic pressure.[10] A nanotextured silica surface with tapered conical pillars, an AR of 5.5 and a period of 200 nm exhibited a superhydrophobic structure with a high pressure robustness of 2.3 MPa and enhanced the broadband optical transmission to over 98% over wavelength band of 500 to 1700 nm.[10] Through these nanopillar arrays, multiple surface functionalities such as antireflection, dust mitigation, and self-cleaning properties can be simultaneously enhanced.[10,13]

While the optical and wetting properties of nanopillar arrays have been investigated in depth, the mechanical properties of these structures are less understood. At the macroscale, nanostructured surfaces can be tested using the cyclic bending test,[14,15] crockmeter test,[16,17] sand abrasion and sandpaper scratching,[18] and normal and shear strength tests with rubber pads and balls.[19,20] At the micro/nanoscale, there have been studies using compression tests *via* an indenter equipped

Walker Department of Mechanical Engineering, The University of Texas at Austin, Austin, TX 78712, USA. E-mail: chichang@utexas.edu

with a flat-end tip on single pillars that are fabricated by focused ion beam milling or lithography combined with reactive ion etching (RIE).[21–27] The mechanical response of 1D silicon nanolines has also been examined and large displacement bursts were observed at different critical loadings due to buckling instability.[28,29] In recent times, 3D nanolattices and mechanical metamaterials with unique mechanical properties, such as improved resilience, stiffness *vs.* density scaling, and negative Poisson's ratio, have been gaining interest.[30–33] The octet-truss unit cell in a nanolattice can make the stretching of the elements the dominant deformation mechanism, resulting in near linear relative *vs.* strength scaling.[34] Ceramic thin-shell nanostructures composed of hollow tubes with a wall thickness of 5–20 nm and a major radius to length ratio of 0.075–0.15 arranged in an octet-truss formation results in shell buckling and exhibit improved ductility and recoverability.[30] Ultrathin nanolattice elements consisting of elements with high ARs result in buckling to increase resilience.[31] However, current studies on the mechanical properties of these nanostructures are limited to 3D nanolattices and not multifunctional surface nanostructures, where the collective behavior of nanostructured arrays is not well understood. As a result, there are unanswered questions regarding the mechanical properties of 2D nanostructures, especially for long-term applications such as optical windows, solar panels, and touch-screen displays.

In addition to structural geometry, the intrinsic material properties also play a key role in the mechanical properties of nanostructured surfaces. One approach for improving mechanical durability is using materials with high constitutive mechanical properties. Of particular interest is sapphire, which is a transparent ceramic with high mechanical hardness, chemical stability, thermal tolerance, and optical transmission. Sapphire is useful for applications such as protective windows,[35] IR optics,[36] camera lenses, sensor covers for aerospace, defense, and consumer electronics industries.[37,38] Silicon is another hard material that is widely used in integrated circuits,[39] photonics,[40,41] and solar panels.[12,42] Both materials have high strength, stiffness, and hardness, but are brittle and prone to crack formation.[35] One method to reduce the brittleness is through scaling to nanoscale, and recent studies have shown that it is possible to observe the brittle-to-ductile transition by decreasing the size of a single, isolated pillar.[22,24,27] However, the question of whether the mechanical response of 2D surface nanostructures can be tuned by the length scale effect remains unanswered.

In this work, we investigate the effect of intrinsic material properties and nanopillar geometry on the deformation mechanisms and mechanical response of periodic surface nanostructures. The depth-dependent mechanical properties of silicon and sapphire nanopillars are characterized *via* quasi-static and cyclic nanoindentation tests. The results show that the deformation behavior of the nanopillar arrays highly depends on the structure AR. We demonstrate that surface nanopillars can be engineered to be compliant and resilient or stiff and hard by tuning the structure AR. The low AR pillars demonstrate enhanced modulus and hardness compared to high AR pillars but are more brittle. The high AR pillars exhibit buckling and structural failure prior to material fracture despite the intrinsic brittleness of the tested material, leading to increased ductility and high resilience. Furthermore, the results reveal that the modulus and hardness of sapphire and silicon show similar degradation trends at increasing AR. Macroscale pencil hardness tests are also used to demonstrate that sapphire structures exhibit scratch resistance while silicon structures experience systematic failure. This work underlines that controlling mechanical properties from high hardness to high resilience is possible through engineering of the pillar geometry, which can lead to the design of multifunctional nanostructured surfaces that are mechanically robust.

II. Experimental methods

The effects of nanopillar geometry and material properties were examined using silicon and sapphire nanopillar array samples with different ARs. The silicon (100) and sapphire (*c*-plane) samples were fabricated *via* interference lithography and the pattern was transferred to underlying substrates using RIE, which have been previously reported.[43,44] The fabricated sapphire nanopillars had a mid-height diameter of 240 nm and a height of 385 nm, resulting in an AR of 1.6, as shown in Fig. 1a. It could be observed that the structure had a cone-like profile with an estimated tip radius of 30 nm. Fabrication of high AR sapphire structures at the nanoscale was difficult to achieve due to the low etch rate selectivity to etching masks due to its mechanical and chemical stability.[45,46] Enhancing the etch rate selectivity requires a multilayer mask, or a hard mask, which in turn increases the process complexity.[43] The low aspect ratio (LAR) silicon nanopillars had a similar profile and had a mid-height diameter of 190 nm and a height of 500 nm, resulting in an AR of 2.6, as shown in Fig. 1b. The high aspect ratio (HAR) silicon nanopillars had a diameter of 125 nm and a height of 1 μm, resulting in an AR of 8, as shown in Fig. 1c. It could be observed that the HAR silicon structure had a more tapered cylindrical profile where the waist of the structure had a slightly smaller diameter. The HAR silicon nanostructures have a broad AR range. A more detailed description of the fabrication process is given in the SI SA.

The fabricated samples were tested *via* a Hysitron TI 950 Triboindenter (Bruker, USA) using a conospherical indenter with a 10 μm tip radius and 90° cone angle. Quasi-static and cyclic nanoindentation test methods were used. The Oliver–Pharr method was employed to calculate the modulus and hardness values.[47] The nanoindentation tests were performed on rectangular arrays consisting of 16 or 25 locations with 20 μm separation to be able to match the test results and the SEM images. The quasi-static tests were performed with different peak loads to measure the mechanical properties at different depths. The sapphire sample was tested at 25

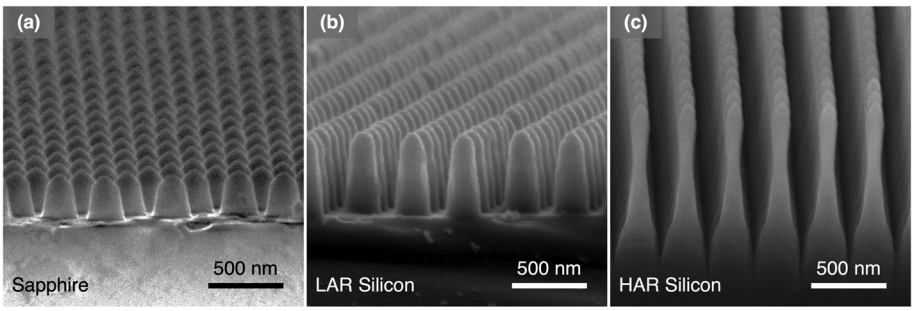

Fig. 1 Cross-section SEM images of (a) sapphire, (b) low aspect ratio (LAR) silicon and (c) high aspect ratio (HAR) silicon nanopillar arrays.

different points, with forces ranging from 100 to 9700 μN. The LAR silicon, similarly, was tested at peak loads from 100 to 9700 μN at 50 different points. The HAR silicon sample was tested at 50, 100 and 1000 μN, at 16 points for each peak load. Due to the structure fracture even at low test loads around 50 μN, the peak load values for each test were kept the same for this sample to avoid densification at higher loads. The cyclic nanoindentation tests were composed of 10 loading and partial unloading cycles with the same maximum load. This approach enabled measuring the mechanical properties at 10 different depths at each test point. The elastic modulus and hardness data were acquired at each segment and the average values were reported with the corresponding standard deviation. For the cyclic testing method, all samples were tested at 16 different points with peak loads of 10.3 mN, 3 mN and 100 μN for the sapphire, LAR and HAR silicon samples, respectively. The detailed calculations for nanoindentation and the load *versus* depth figures of raw indentation results for all the samples are provided in the SI SB.

The scratch resistance of the samples was evaluated using an Elcometer 501 pencil hardness tester (Elcometer, UK) by following ASTM D3363. Due to small sample size, only pencils with hardness 4B, 2B, 2H and 6H were used to test the sapphire sample, and 2B pencil was used for the silicon samples. After the scratch test, the sample was cleaned in deionized water with sonication, followed by piranha solution cleaning, RCA cleaning, and oxygen plasma cleaning to remove the graphite residue.

III. Results and discussion

A. Nanoindentation test results

The representative quasi-static and cyclic nanoindentation load *vs.* depth graphs for sapphire, silicon LAR and HAR samples are shown in Fig. 2. The inset images depict the top-view SEM images at various regimes of the indents, which differs by the structure material and AR. A schematic illustration summarizing the distinct deformation regimes of LAR and HAR nanopillars is provided in Fig. S3. Sapphire nanostructures show a relatively smooth mechanical response, as shown in Fig. 2a. Most notably it does not exhibit an explicit pop-in region, which are typically observed in nanoindentation of bulk sapphire,[48] indicating an improvement in ductility. The inset SEM image shows that brittle fracture has occurred in a few of the pillars at the center of the indent, but the cracks do not propagate into the sapphire substrate. It can be noted that the pillars are mostly intact, and their shapes do not change considerably. In this experiment, the maximum indentation depth is around 125 nm, or 1/3 of the total structure height, therefore the substrate is expected to have an effect. The curve from the cyclic loading can is similar to the quasi-static loading with low hysteresis effects observed.

The silicon LAR nanopillars are indented to a larger depth relative to their height, and exhibit three distinct deformation regimes, as shown in Fig. 2b. In the first regime, a similar behavior to sapphire where the displacement increases monotonically with force is observed. This linear response is observed until around 3 mN load, after which a pop-in event occurs, indicating a sudden change in displacement. SEM imaging of the sample indicates that the pop-in is a result of the initiation of pillar fracture, as shown in the corresponding inset image given in Fig. 2b(i). Increasing the load further leads to the second regime and results in a large pop-in with roughly 100 nm of additional displacement, which can be attributed to systematic fracture of the Si structures. The pop-in is readily observable in the inset image of Fig. 2b(ii), where multiple pillars are broken and removed. The rapid change from elastic deformation to fracture underlines the brittle nature of silicon. Regime three is densification and starts after the larger pop-in, where the load increases in a smoother manner with multiple smaller pop-ins observed. The corresponding SEM image indicates that more pillars at the periphery of the indentation region are broken and the pillars at the center are densified, as shown in Fig. 2b(iii). It can be noted that unlike the sapphire nanostructures which has a smooth, monotonic response, the silicon nanostructures undergo distinct systematic fracture and densification regimes. Smaller pop-ins are observed during the first regime of LAR silicon sample at indentation loads below 3 mN, after which point, the large pop-in occurs. During these small pop-ins, pillar splitting and fracture from the bottom of the pillar is observed. In the sapphire sample, while pillar splitting is observed, as seen in Fig. 2a(i) and d(i), distinct pop-ins and fractures from the pillar base are not

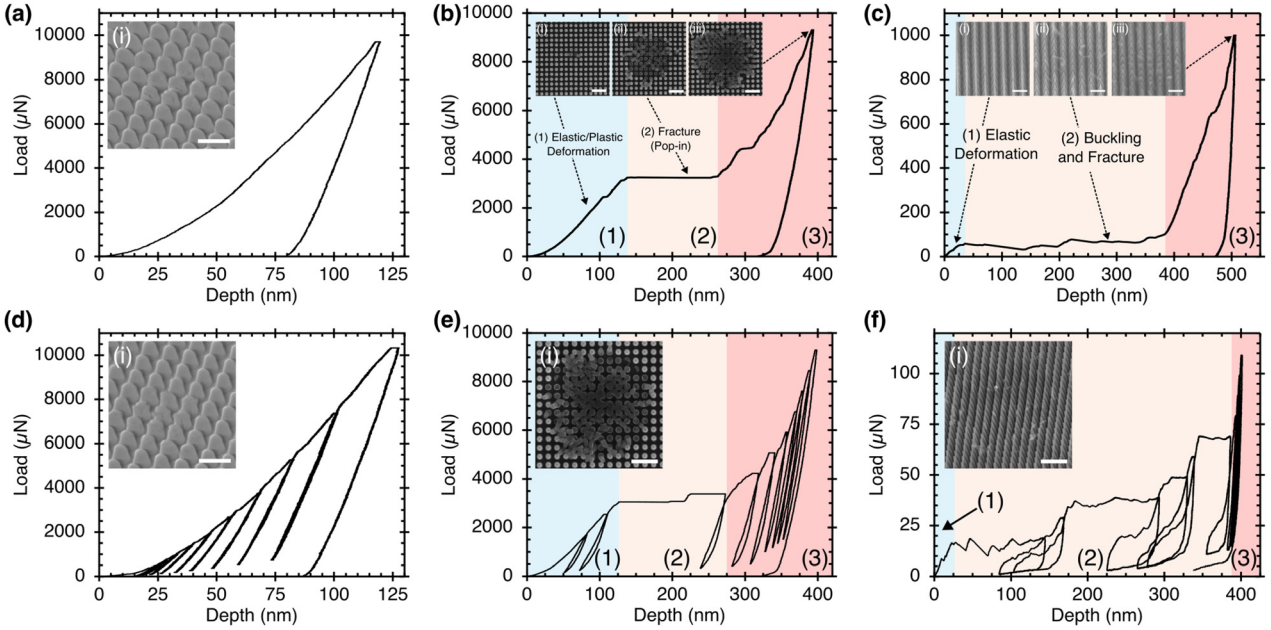

Fig. 2 Load-depth graphs of quasi-static and cyclic nanoindentation tests on (a and d) sapphire, (b and e) LAR silicon, and (c and f) HAR silicon nanostructures. The insets are representative images showing indented regions at different locations, at the maximum depth shown with the arrow. Scale bars of inset SEM images: (a, c and d) 500 nm and (b, e and f) 1μm.

observed. These results illustrate that sapphire and silicon nanopillar arrays behave differently under compressive loading even though the pillars have similar aspect ratios. It can also be noted that at the maximum load of 10 mN, the highest available for the nanoindentation system, the indention depth into sapphire is much shallower than that of the LAR silicon due to the high stiffness of the sapphire nanostructures.

The load *versus* displacement graph for the HAR silicon sample is given in Fig. 2c. Similar to the LAR silicon, this sample exhibits three distinct deformation regimes as well. The deformation mechanism of this sample includes a local strain of the structure at low depths up to tens of nanometers. In this regime, the deformation is elastic, and no permanent strain can be observed, as shown in the inset SEM image in Fig. 2c(i). In the second regime, at intermediate loads, the pillars buckle and/or bend, leading to large strain and a ductile-like response. At increasing loads, the pillars fracture through bending. The nanopillars typically fracture at the waist of the structure where the diameter is the smallest, as shown in the inset image Fig. 2c (ii). The buckling of these structures is modeled and described further in the following section. In the third regime, densification of the nanopillars is observed at higher indentation depths. This leads to a higher stiffness as calculated from the slope of the unloading part of the load *vs.* displacement curve, as observed in cyclic tests. The inset image Fig. 2c(iii) shows the collapse and fracture of the broken structures. Note that the second regime of structure buckling leads to geometry-induced ductility in the mechanical response and is not observed in the sapphire and LAR silicon samples.

The indentation modulus and hardness can be calculated from the load–displacement curves and plotted against depth for all three samples, as shown in Fig. 3. For the sapphire sample, the modulus and hardness values at each maximum load are in good agreement between the quasi-static tests and cyclic tests, as shown in Fig. 3a and d, respectively. To minimize the substrate effect, a common rule of thumb is to use less than 10% of the film thickness for thin film samples.[49] A similar approach is followed and ~10% of the total pillar height, a maximum indentation depth of 68.7 ± 5.5 nm, is considered. The modulus and hardness for the sapphire nanostructures at this depth are 131.1 ± 6.9 GPa and 2.14 ± 0.18 GPa, respectively. Both values increase at higher indentation depths for the sapphire sample, until leveling out at around 80 nm depth where the modulus and hardness reach up to 170.9 ± 10.3 GPa and 3.73 ± 0.67 GPa, respectively. These values are smaller but have not significantly degraded compared to bulk sapphire, which has modulus and hardness of 440 GPa and 30 GPa, respectively.[47,48]

In comparison with sapphire, the LAR silicon structures are not as stiff or hard. The LAR silicon has modulus and hardness of 53.4 ± 2.7 GPa and 1.02 ± 0.14 GPa at a 104.6 ± 9.2 nm indentation depth, as shown in Fig. 3b and e, respectively. Both values then gradually decrease as the load increases, corresponding to the onset of structural fracture. In comparison, bulk silicon has a modulus and hardness of 169 GPa and 14.2 GPa, respectively.[50,51] After indentation to a 200 nm depth, the hardness levels out at around 0.4 GPa. Note that a sudden change in hardness is observed at 100 nm, which is the onset of the cascade collapse (LAR regime 2), followed by the systematic, rapid fracture resulting in fewer data points between 100 and 250 nm, as shown in Fig. 3b. This behavior is also seen in Fig. 2b, indicating a sudden fracture of multiple

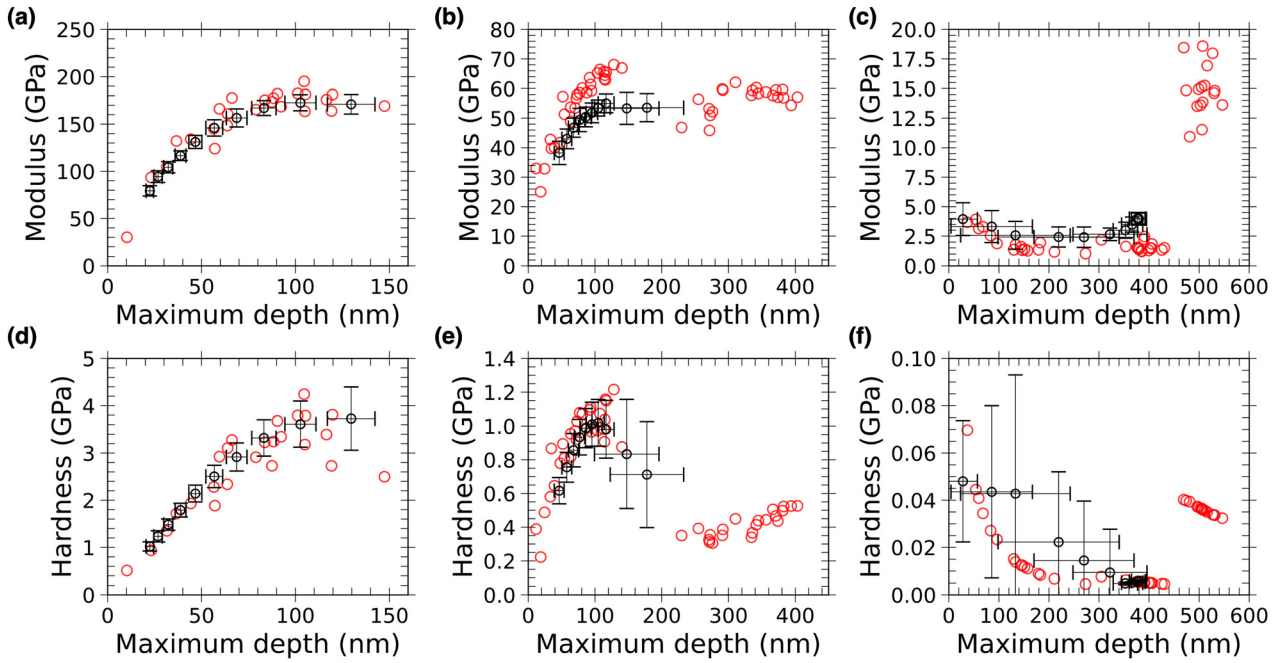

Fig. 3 Indentation modulus *versus* depth graphs for (a) sapphire, (b) LAR silicon and (c) HAR silicon nanostructures. Measured hardness *versus* depth graphs for (d) sapphire, (e) LAR silicon, and (f) HAR silicon nanostructures. Red and black circles show quasi-static and cyclic test results, respectively. Error bars show one standard deviation.

silicon pillars. The indentation modulus increases gradually until a 120 nm depth, leveling out around 55 GPa. Unlike the sapphire sample, there is a difference between the results of the cyclic and single point tests. This deviation rises as the indentation depth increases, indicating the brittle nature of the material since material response changes after each loading and unloading segment due to cracks forming in pillars reducing the indentation modulus.

On the other hand, the taller HAR structures have a more compliant response. The HAR silicon sample has a modulus and hardness of 3.94 ± 1.39 GPa and 48.0 ± 25.7 MPa, at a 28.2 ± 28.7 nm indentation depth, as shown in Fig. 3c and f, respectively. Large variation can be observed for the indentation data, which can be attributed to the sensitivity of buckling/bending to small variations in the structural geometry, where the average waist diameter is 45.5 ± 8.6 nm, and the diameter distribution is provided in Fig. S8. Unlike the other two cases, HAR silicon nanopillars have higher hardness and indentation modulus at lower indentation depths, which then decrease with increasing depth. This behavior can be attributed to the onset of structure buckling (HAR regime 2), which occurs at around 25 nm. However, there is an improvement in modulus after 300 nm of indentation depth due to densification (HAR regime 3). It can be observed that the load–displacement curves on the HAR show abrupt and unpredictable fractures. This behavior can be attributed to the considerable influence of small variances in diameter on the critical buckling force and explored further in the following paragraphs. As a result, HAR nanopillars fracture unpredictably, causing the high standard deviation in the mechanical properties, as can be observed in Fig. 3f.

B. Compressive cascade failure of LAR nanopillars

To better understand the mechanical response of the silicon nanopillars, it is important to examine the deformation mechanism and failure modes. For the LAR silicon pillars, there is a sudden change in hardness between 100 and 250 nm where the pillars suddenly collapse, as shown in Fig. 3e. The sudden fracture of multiple pillars is also observed in Fig. 2e. At the first pop-in, the conospherical probe exerts mostly compressive load on the center pillar, causing it to split, as shown in Fig. 4a. In contrast, the pillars at the outer region are subjected to bending and shearing loads due to off-axis loading. After the brittle fracture of the center pillar, the average load on the remaining pillars increases rapidly. This sudden load increase on the remaining pillars causes a cascading fracture that progresses radially outward from the center pillar, as shown in Fig. 4b. Furthermore, while first few pillars are fractured through splitting, the outer pillars fracture closer to their root. Another cause of this behavior is that the broken pillars are pushed towards the unbroken pillars during the cascading fracture, causing an off-axis loading due to the shape of the conospherical indenter.

To estimate the compressive strength of an individual pillar, the stress each pillar is subjected to is calculated by using the geometry of the indenter. The deformation of each pillar is calculated by assuming that the indenter is a perfect sphere and does not deform during indentation. Moreover, the

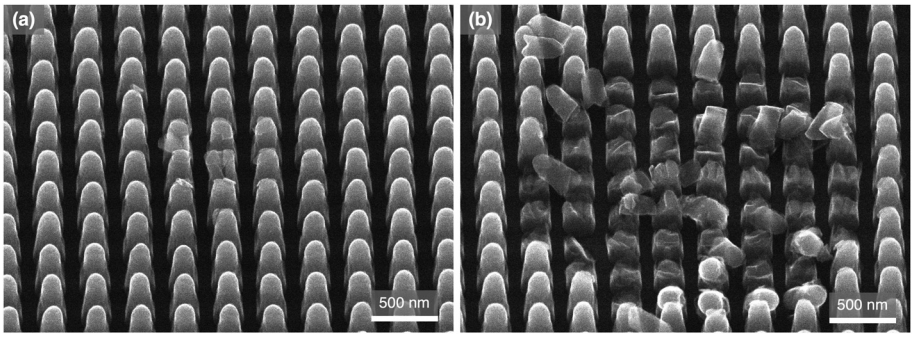

Fig. 4 SEM images of indented regions of the LAR silicon sample. The image in (a) shows the splitting single pillar, and (b) shows the fracture at roots of the pillars after cascading fracture.

load exerted by the indenter is distributed to the pillars according to the indentation depth. This approach assumes that the force exerted on a pillar is proportional to its deformation. Using this method, the fracture strength of the pillars can be approximated by calculating the compressive stress in the split center pillar, which is approximately 4 GPa. This value is comparable to the compressive strength of 6–8 GPa reported for single isolate silicon micropillars in the literature.[21–23] In comparison, the compressive strength of the sapphire is much higher at 10.9 GPa. More detailed description of the pillar stress estimation is described further in the SI SC.

C. Buckling and bending failure of HAR pillars

In contrast to compressive fracture, buckling-induced bending failure can be observed in the HAR nanopillars. During the indentation, the pillar at the center is mostly subjected to compressive loading, causing buckling of the pillars. It is important to note that the off-center pillars are also subjected to bending due to the lateral forces, as discussed further in the SI SD. Both deformations can be highly recoverable due to slender pillar geometry and the diameter of the pillars, resulting in the pillars returning to the vertical position upon tip unloading. In HAR regime 1, the quasi-static nanoindentation test of the HAR silicon sample with a 50 μN maximum load at two locations is shown in Fig. 5, which resulted in different indentation depths of 38.6 and 133.5 nm. It can be observed that for the shallower indentation depth with AR ~ 7, the structures do not undergo buckling and can have complete recovery with no broken pillars, as shown in Fig. 5a and b. For the regions with deeper indentation as a result of smaller nanopillar neck and higher AR ~ 10, some broken pillars can be observed due to buckling and fracture, as shown in Fig. 5c. Nevertheless, a recovery of 52% is observed upon unloading and most pillars are intact. This high resilience can be attributed to the distinct buckling and bending deformation mechanisms for the HAR silicon structures. The recovery of the nanopillars can be observed in the corresponding SEM image shown in Fig. 5d, where the pillars near the center (denoted by arrows) are intact after unloading. It can be observed that their neighboring pillars, some further away from the center of the indent region, are broken. This behavior shows that these pillars buckled during indentation, but are able to rebound to their initial shape upon unloading. This is due to the high AR and smaller diameter of these pillars, making the critical load for buckling lower than the critical load for material fracture. There are other nanopillars on the edge of the fractured region, which is much smaller than the expected indentation region of 3.25 μm, indicating that they also buckled or bent and sprung back. The recovery is not observed in all HAR silicon pillars, some of which have fractured at the waist due to the bending stress exceeding the strength of the material after buckling. This non-uniform effect can be attributed to the pillars having slightly different waist diameters, which influences the deformation behavior of each pillar. If the pillar diameter is large enough, the structure AR is reduced and fracture due to bending may be observed. As the structure AR increases, their ability to buckle without brittle fracture improves.

These results indicate that the AR plays a critical role in the deformation and failure mechanism, namely brittle fracture for LAR and buckling/bending for HAR structures. In the low AR regime, the fracture strength can be related to the intrinsic compressive strength of the pillar, which is estimated to be around 6–8 GPa based on literature values of similar size Si pillars.[21,23] While the compressive strength can be size dependent, here it is assumed to be constant for the different pillars since the diameter does not vary significantly for the LAR samples. At high AR, the buckling and bending failure can be approximated using classic Euler buckling.[52] In this model, the critical stress to induce buckling for uniaxial compression is given as $\sigma_{cr}^{b} = \frac{\pi^2 E}{16AR^2}$, where E is the elastic modulus of the material, and AR is the aspect ratio of a pillar, defined as AR = h/d and h and d are the length and the diameter of a pillar, respectively. The critical aspect ratio, $(AR)_c$, can be defined by setting the two equations to be the same to find the boundary of the two deformation modes and is calculated as 4.17. In this model, pillars with a higher aspect ratio have buckling failure and the pillars with a lower value have fracture due to excessive compressive stress. More details on the failure mode modeling are given in the SI SD.

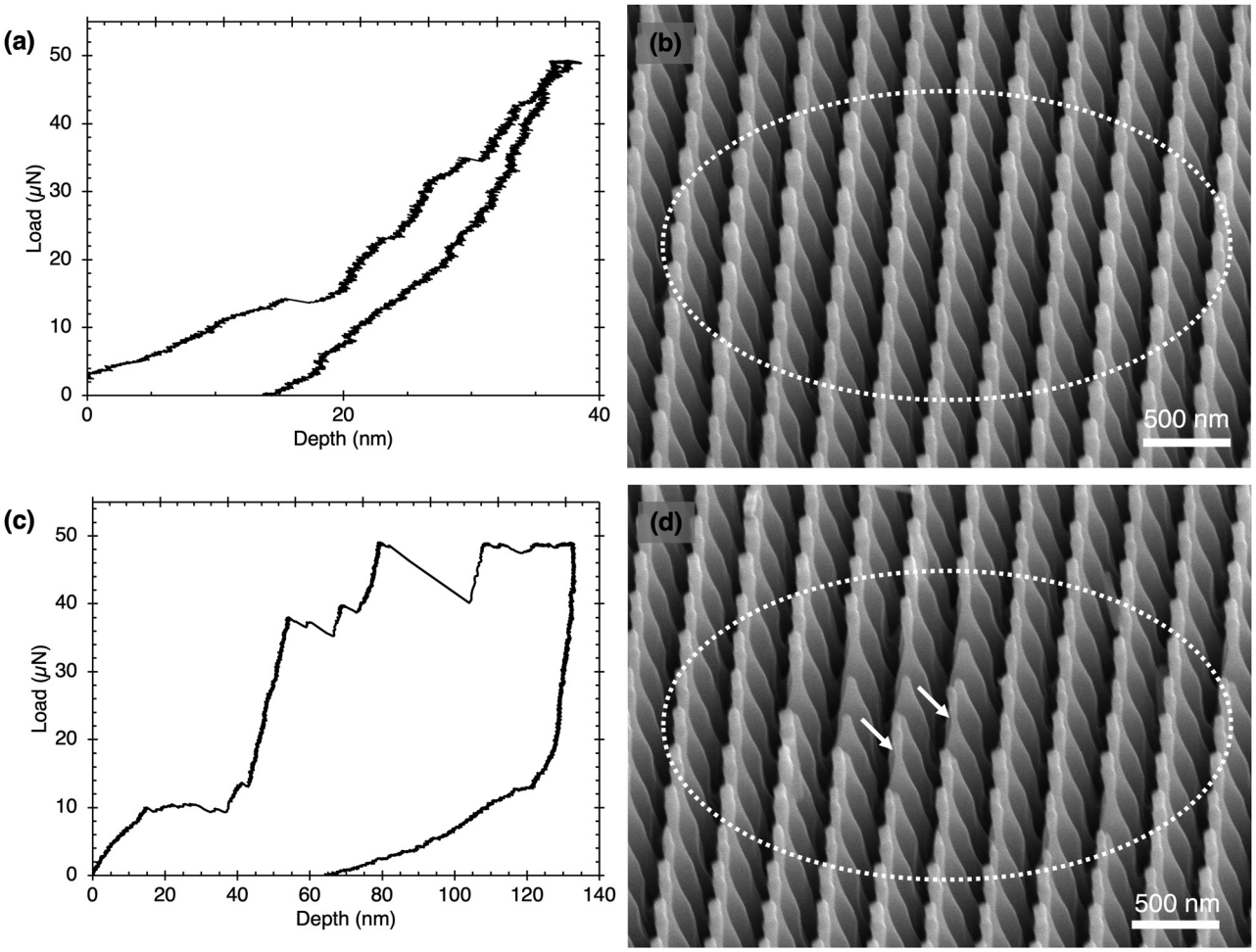

Fig. 5 Load displacement graph and SEM images of test regions of HAR silicon nanopillars at 50 μN. (a and b) Nanoindentation test with no broken pillars in the tested area as shown with dashed lines. (c and d) Nanoindentation test of a region with broken and recovered pillars. The arrows denote two recovered nanopillars with aspect ratios of 9.7 and 12.4 (from left to right). The dashed lines show the approximate footprint of the indented region.

The failure diagram of compressive stress *vs.* pillar aspect ratio for both fracture and buckling modes are illustrated in Fig. 6a. Using the SEM images, the AR of the LAR silicon nanopillars with the smallest diameter is calculated as 2.5, which is below $(AR)_c$. According to this model, the main deformation mode for LAR silicon nanopillars is material fracture due to compressive loading without any buckling. The model agrees with the compressive fracture of the LAR nanopillars observed at around 3 mN, as shown in Fig. 4. As described in previous sections, this load corresponds to a compressive stress of ~4 GPa for the central pillar at the initiation of the cascade fracture. Note that this strength is slightly lower than the literature value of 6–8 GPa, which can be attributed to shear stresses since the indentation is not uniaxial. The aspect ratios of the HAR silicon nanopillars are calculated as 5.8 and 14.8 for the largest and smallest diameters, respectively. It can be noted that HAR pillars have higher variations in aspect ratio compared with LAR pillars, as illustrated by the shaded regions in the diagram. The test results shown in Fig. 6a have corresponding stresses at buckling and the end of HAR regime 1 in the force–displacement response between 0.7 GPa and 2.5 GPa. It can be observed that for these samples, the AR is above the $(AR)_c$; therefore, the main failure mode for HAR silicon nanopillars is buckling. It is important to note that the failure diagram captures only the onset of fracture for LAR and buckling for HAR, which is the end of the first deformation regimes in both cases, and does not describe the later regimes such as systematic fracture and densification. Details on the calculation of buckling stress are given in the SI SD.

The dependency of the indentation modulus and hardness *vs.* the aspect ratio of the nanopillar arrays is also strong, as shown in Fig. 6b and c, respectively. The relative densities of the sapphire, LAR and HAR silicon nanostructures are estimated by averaging the volume of the nanopillar structures, which are 0.35, 0.28, and 0.21, respectively. Note that the tapered profile results in a changing volume fraction *versus* depth, and the current estimate is based on the entire height. Empirical fitting of the nanopillar moduli normalized by the

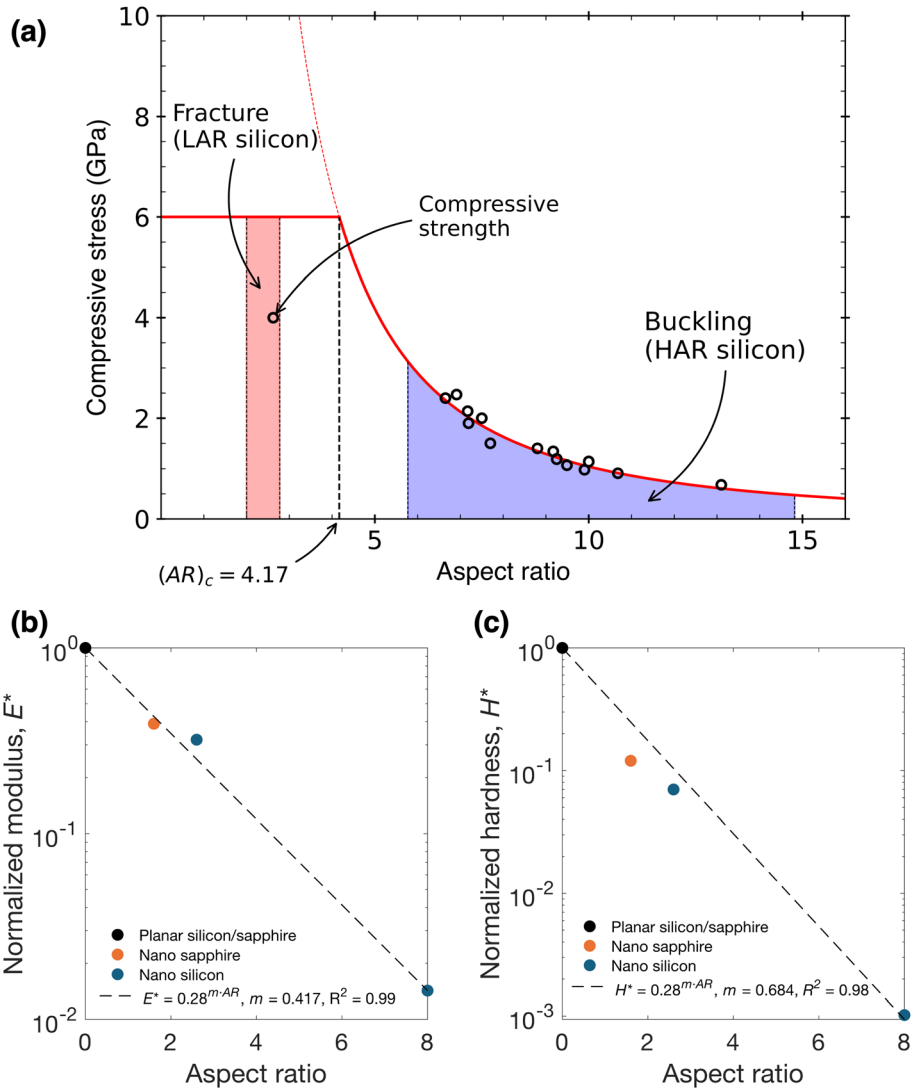

Fig. 6 (a) Critical stress for fracture and buckling/bending failure modes due to compressive normal stress *versus* AR for silicon nanopillars. LAR is in the fracture region while HAR silicon is in the buckling region. Normalized indentation (b) modulus and (c) hardness *versus* nominal AR for sapphire and silicon nanostructures.

moduli of bulk sapphire and silicon *vs.* AR is given in the form of $E_{\text{norm}} = \rho^{m \times \text{AR}}$, where ρ is the average density of 0.28 for all samples, m is the fitted exponent and AR is the aspect ratio. Therefore, the value of m shows the sensitivity of the material properties to the changing aspect ratio, where a lower value indicates lower degradation with increasing AR. It can be noted that both values decrease with increasing AR. It is interesting to note that the degradation in modulus and hardness relative to their bulk properties is similar for both silicon and sapphire. It can also be noted that hardness is more sensitive to AR compared to modulus in both cases due to the structural failure mechanism. Additional experiments at a broader range of densities and AR for both silicon and sapphire are needed to further quantify the intrinsic material effects. More details of the density scaling calculation are described in the SI SE.

D. Macroscale scratch testing

To further evaluate the scratch resistance of the sapphire and silicon nanostructures, the samples are tested with the standard ASTM D3363 pencil hardness testing method. In this test, a graphite pencil with known hardness is pressed on the sample with a 7.5 N force and pushed laterally. The samples with pencil marks and their SEM images are provided in Fig. 7. The sapphire structures are first tested using a 2B pencil, since the hardness of the sapphire sample was found to be as high as 3.7 GPa and is expected to withstand the scratch. The scratch mark of the sample is shown in the microscopy image shown in Fig. 7a, where the test area is covered with graphite. This result demonstrates that the sapphire nanostructures have higher hardness and the pencil tip is scratched. The scratched area is examined under the SEM,

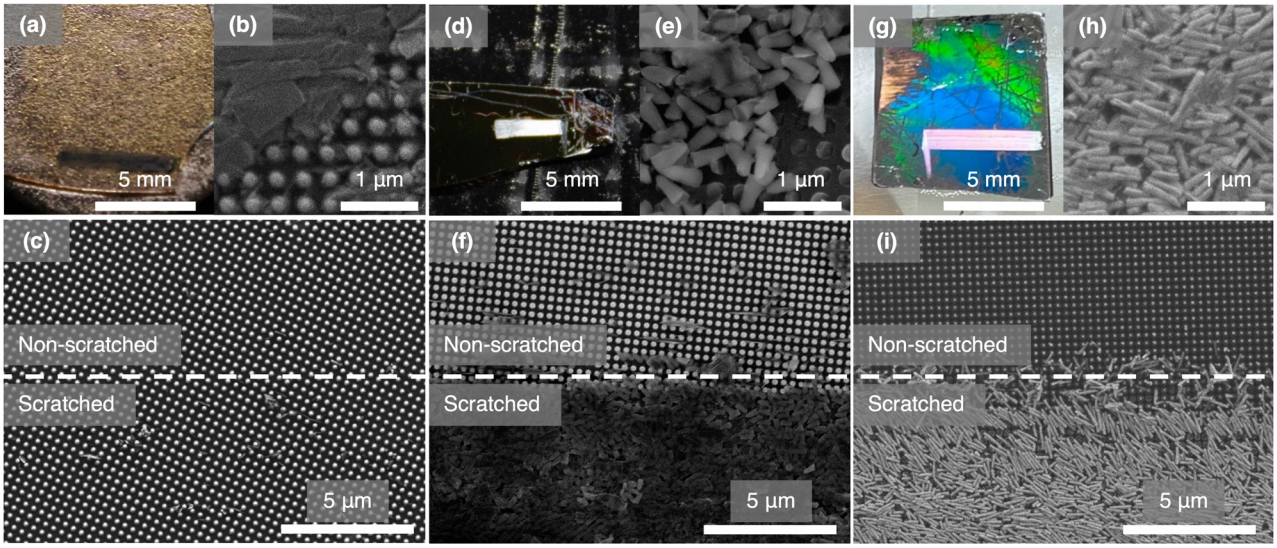

Fig. 7 The optical micrograph and SEM images of the nanopillar samples after pencil hardness testing with 2B pencil. Images (a–c) show the sapphire, (d–f) show the LAR and (g–i) show the HAR silicon samples. (c, f and i) The SEM images of the edge of the scratched and non-scratched areas, where the dashed lines show the boundary.

showing the intact sapphire pillars under the graphite debris, as shown in Fig. 7b. After the debris is removed using piranha and RCA cleaning, the boundary of the scratched and non-scratched areas is examined under the SEM, as shown in Fig. 7c. It can be observed that the difference between the two areas is not noticeable, and the pillars have not affected by the pencil test. Note that there are still a few graphite debris remaining between the pillars in the scratched area. The analysis of the entire scratch area spanning 6 mm by 0.7 mm indicates that more than 96% of the pillars were intact after the pencil hardness test. The sample was also tested with higher hardness pencils including 2H and 6H, which shows higher percentage of damaged sapphire structures. These results and detailed analysis of the scratch test and yield results are described further in the SI SF.

For direct comparison with the sapphire nanostructures, the LAR silicon sample is also tested using the 2B pencil. The scratched sample shows a shiny surface, as shown in Fig. 7d, which implies that most of the pillars are broken; hence, the nanostructure lost its antireflection properties. These results are expected since the hardness of the LAR pillar is found to be around 0.6 GPa at the indentation depth of ~10% of the pillar height and much lower than those of the sapphire samples. The broken pillars can be observed in the SEM image of the test area, as shown in Fig. 7e. Also, there is a clear boundary between the scratched and non-scratched regions, where pillars are intact in the former and are all broken in the latter, as shown in Fig. 7f. A bit of graphite debris can be observed in the broken LAR pillars, indicating that the pencil tip was also scratched during the test The HAR silicon pillars have a lower measured hardness of 48 MPa and is also tested with a 2B pencil. Similar to the LAR silicon pillars, a shiny surface appears after the pencil testing, as shown in Fig. 7g. It can be observed that all of the silicon nanopillars are broken in the scratched area, as shown in the SEM micrograph in Fig. 7h. Also, the boundary between the scratched and non-scratched areas is observable, as shown in Fig. 7i. However, it is interesting to note that there is almost no graphite debris, indicating that the pencil tip has a much higher hardness than the HAR silicon nanopillars as expected.

E. Discussion and future work

The nanoindentation and pencil scratch testing results indicate that both the material and AR of the nanopillars influence the mechanical behavior. Sapphire provides a higher hardness and indentation modulus compared to silicon nanostructures at similar aspect ratios and is more scratch resistant. The sapphire sample has a 170.9 ± 10.3 GPa indentation modulus and a 3.73 ± 0.67 GPa hardness, while the LAR silicon sample exhibits a 53.4 ± 2.7 GPa indentation modulus and a 1.02 ± 0.14 GPa hardness. Sapphire nanostructures perform better than LAR silicon with 3.2 times higher moduli and 3.6 times higher hardness. HAR silicon samples are more compliant and exhibit indentation modulus and hardness of 3.94 ± 1.39 GPa and 48.0 ± 25.7 MPa, respectively. Therefore, the LAR silicon sample has 13.6 times higher modulus and 21.3 times higher hardness compared to the HAR sample. LAR silicon nanopillars exhibit better mechanical performance in terms of hardness and stiffness but they are brittle, while HAR structures are softer but more resilient, exhibiting recoverable deformation due to buckling. Compared to their intrinsic material properties, the LAR silicon sample maintains 32% of the modulus and 7% of the hardness, while the sapphire sample maintains 39% of the modulus and 12% of the hardness. Therefore, using a material with better intrinsic material

properties is crucial to obtain more mechanically robust nanostructured surfaces.

Using nanoindentation test results, it is possible to compare the performance of the nanostructured sapphire with current optical windows, protective covers and antireflective surfaces. Soda-lime glass is a widely used optical window material, and has a nanoindentation hardness of ~6 GPa.[47] Magnesium fluoride (MgF_2) is a material used as an antireflective coating (ARC), which can achieve a nanoindentation hardness of 9 GPa and a modulus of 132 GPa.[53] Therefore, the hardness of the presented nanostructured sapphire lies close within the range of commercially available optical windows and classical ARCs. Further enhancements in hardness could be obtained by decreasing the nanopillar height of sapphire nanostructures. The experimental results of HAR and LAR silicon nanopillars show that hardness increases with decreasing pillar height. Optical simulations show that decreasing the height to ~150 nm does not hinder the antireflection performance within the visible range. Therefore, shorter sapphire nanopillars would provide better hardness while enhancing antireflection.

While these experiments demonstrate a strong effect of the structure AR on the mechanical response of the nanopillars, further investigation into the influence of the size effect is needed. For example, the compressive strength of the nanopillars, which is assumed to be constant in our model, can increase as the diameter decreases and reaches below 50 nm.[21,23,25,26,54] The thin silicon nanopillars can demonstrate anelasticity and the transient response needs to be examined as it could be one of the recoverable deformation mechanisms in HAR silicon.[55] Moreover, the presented mechanical model approximates the load applied uniaxially and bending and shearing stresses can also be introduced due to the spherical indenter geometry. As future work, a finite element analysis model of the nanoindentation tests will be employed to further understand the multiaxial deformation mechanisms. Moreover, *in situ* testing for HAR nanostructures will shed light on the exact deformation mode of the structures. Fabrication and testing of lower AR silicon and sapphire samples could generate nanopillar arrays with mechanical performance similar to the bulk material properties. The co-designing of optical and mechanical properties needs to be investigated in depth for designing mechanically robust optical surfaces.

IV. Summary

In this work, we demonstrated that by designing the AR of the nanopillars, it is possible to control the mechanical response of the nanopillar arrays. Low AR nanopillars generate stiff and hard surface nanostructures, but are more brittle and can fracture. Specifically, the sapphire nanostructures with low AR demonstrated a 170.9 ± 10.3 GPa indentation modulus and a 3.73 ± 0.67 GPa hardness using nanoindentation tests. Despite having a nanostructured surface, the sapphire sample demonstrated its mechanical robustness in the pencil hardness test, where over 96% of the pillars remained intact after scratching with a 2B pencil with a 7.5N load. On the other hand, high AR silicon nanopillars are compliant and prone to scratches but are highly resilient and can exhibit recoverable deformation of over 50% recovery upon unloading. The findings will help guide the design and fabrication of mechanically robust nanostructured materials with fine-tuned surface properties for applications in nanophotonics, multifunctional surfaces, and displays.

V. Methods

A. Fabrication

Sapphire. Initially, a 100 mm sapphire substrate (single crystal, *c*-plane) was deposited with a 1 μm-thick polysilicon layer using low-pressure chemical vapor deposition (LPCVD) as the etch mask. The samples were spin coated with a 100 nm-thick antireflection coating (Brewer Science, ARC i-con-7) to reduce back reflection during lithography and then coated with a 200 nm-thick photoresist (Sumitomo, PFi-88A2). A Lloyd's mirror interference lithography setup with a HeCd laser (325 nm wavelength) was used to pattern a 2D pillar array in a square lattice with a period of 330 nm. The photoresist pattern was transferred into the underlying antireflection coating, polysilicon, and sapphire substrates using inductively coupled plasma reactive ion etching (ICP-RIE) with an Oxford 100 system (Oxford Instruments, UK) using O_2, HBr, and BCl_3/HBr gases, respectively. This process involves obtaining polysilicon nanopillars to fabricate large-area and periodic sapphire nanostructures with high aspect ratios.[43]

Silicon. Initially, a 100 nm antireflection coating (ARC, i-con-7, Brewer Science) was spin-coated on the silicon substrate. A 200 nm photoresist (PFI-88A2, Sumitomo) was then spin-coated on the antireflection coating layer. The photoresist was exposed using Lloyd's mirror interference lithography to form 2D patterns with a period of 300 nm in the photoresist layer. The patterned structures were transferred to the underlying substrate using ICP-RIE etching with an Oxford 100 system (Oxford Instruments, UK). To transfer the photoresist pattern into antireflection coating and silicon substrates, O_2, and HBr gases were used, respectively. After completing the etching process, the remaining photoresist and antireflection coating above the silicon nanostructures are cleaned *via* wet or dry-cleaning processes such as RCA Clean or O_2 ICP-RIE. The high aspect ratio (HAR) nanopillars are fabricated through low RF power during the HBr RIE process.[44]

B. Nanoindentation

Nanoindentation measurements were performed using a Hysitron TI 950 Triboindenter (Bruker, USA). A conospherical indenter with a 10 μm tip radius and 90° cone angle was used. The loading rates of 1 mN s^{-1} for sapphire, 200 μN s^{-1} for LAR, and 20 μN s^{-1} for HAR silicon were kept the same within the same sample. The load and displacement data were

recorded at a 200 Hz data acquisition rate. During the partial unloading sections in cyclic tests, the load was decreased to 10% of the peak load of the segment. The hardness and indentation modulus data of the cyclic tests were calculated for the same peak load segment. Mean and standard deviation values of maximum depth, hardness and modulus were calculated for the same peak load segment.

C. Pencil hardness test

The scratch resistances of the samples were evaluated using an Elcometer 501 pencil hardness tester (Elcometer, UK) by following ASTM D3363 (Standard Test Method for Film Hardness by Pencil Test). After the pencil test, the sample was cleaned in deionized water with sonication. It was then cleaned in piranha solution (concentrated H_2SO_4 and 30% H_2O_2 solution with 2 : 1 volume ratio) at 100 °C for 15 minutes and RCA (5 : 1 : 1 volume ratio of deionized water, NH_4OH, 28–30% NH_3 basis, and 30% H_2O_2 solution) cleaning at 80 °C for 30 minutes. The sample was then cleaned in O_2 plasma etching at 18 W and 500 mTorr for 10 minutes.

Author contributions

C.-H. C. and M. K. conceived the presented idea. K.-C. C. and K. S. L. fabricated the experimental samples. M. K. performed the experiments, formulated the deformation mechanisms, and wrote the initial draft of the manuscript. M. K., N. A. R. G., and C.-H. C. contributed to writing, review, and editing. C.-H. C. secured funding and supervised the project.

Conflicts of interest

There are no conflicts to declare.

Data availability

The data supporting this article have been included as part of the supplementary information (SI). Supplementary information is available. See DOI: https://doi.org/10.1039/d5nr05216e.

Acknowledgements

This work was performed at UT Austin Texas Materials Institute (TMI) and the Texas Nanofabrication Facility, which is supported by the National Science Foundation (NSF) as part of the National Nanotechnology Coordinated Infrastructure (NNCI) grant NNCI-2025227. This work is funded by the National Aeronautics and Space Administration (NASA) under grant 80NSSC25K7279, the Army Research Office (ARO) under grant W911NF-22-1-0124, and the National Science Foundation (NSF) under grant TI-2314268.

References

1 P. B. Clapham and M. C. Hutley, *Nature*, 1973, **244**, 281–282.
2 S. J. Wilson and M. C. Hutley, *Opt. Acta*, 1982, **29**, 993–1009.
3 W. Barthlott and C. Neinhuis, *Planta*, 1997, **202**, 1–8.
4 M. Zhang, S. Feng, L. Wang and Y. Zheng, *Biotribology*, 2016, **5**, 31–43.
5 D.-H. Ko, J. R. Tumbleston, K. J. Henderson, L. E. Euliss, J. M. DeSimone, R. Lopez and E. T. Samulski, *Soft Matter*, 2011, **7**, 6404–6407.
6 Y.-F. Huang, S. Chattopadhyay, Y.-J. Jen, C.-Y. Peng, T.-A. Liu, Y.-K. Hsu, C.-L. Pan, H.-C. Lo, C.-H. Hsu, Y.-H. Chang, C.-S. Lee, K.-H. Chen and L.-C. Chen, *Nat. Nanotechnol.*, 2007, **2**, 770–774.
7 G. Tan, J.-H. Lee, Y.-H. Lan, M.-K. Wei, L.-H. Peng, I.-C. Cheng and S.-T. Wu, *Optica*, 2017, **4**, 678–683.
8 F. Xia and L. Jiang, *Adv. Mater.*, 2008, **20**, 2842–2858.
9 S. Haghanifar, M. McCourt, B. Cheng, J. Wuenschell, P. Ohodnicki and P. W. Leu, *Mater. Horiz.*, 2019, **6**, 1632–1642.
10 K.-C. Park, H. J. Choi, C.-H. Chang, R. E. Cohen, G. H. McKinley and G. Barbastathis, *ACS Nano*, 2012, **6**, 3789–3799.
11 W. H. Southwell, *J. Opt. Soc. Am. A*, 1991, **8**, 549–553.
12 J. Cai and L. Qi, *Mater. Horiz.*, 2015, **2**, 37–53.
13 K.-C. Chien, M. Kepenekci, A. Tunell and C.-H. Chang, *Mater. Horiz.*, 2025, **12**, 1796–1807.
14 S.-F. Leung, L. Gu, Q. Zhang, K.-H. Tsui, J.-M. Shieh, C.-H. Shen, T.-H. Hsiao, C.-H. Hsu, L. Lu, D. Li, Q. Lin and Z. Fan, *Sci. Rep.*, 2014, 1–8.
15 M. Finn, C. J. Martens, A. V. Zaretski, B. Roth, R. R. Søndergaard, F. C. Krebs and D. J. Lipomi, *Sol. Energy Mater. Sol. Cells*, 2018, **174**, 7–15.
16 J. Rombaut, R. A. Maniyara, R. A. Bellman, D. F. Acquard, A. S. Baca, J. Osmond, W. Senaratne, M. A. Quesada, D. Baker, P. Mazumder and V. Pruneri, *ACS Appl. Mater. Interfaces*, 2018, **10**, 43230–43235.
17 I. Karadzhov, B. Paulillo, J. Rombaut, K. W. Koch, P. Mazumder and V. Pruneri, *ACS Appl. Mater. Interfaces*, 2024, **16**, 19672–19680.
18 S. Dong, Z. Wang, Y. Wang, X. Bai, Y. Q. Fu, B. Guo, C. Tan, J. Zhang and P. Hu, *ACS Appl. Mater. Interfaces*, 2018, **10**, 2174–2184.
19 J.-G. Kim, H. J. Choi, K.-C. Park, R. E. Cohen, G. H. McKinley and G. Barbastathis, *Small*, 2014, **10**, 2487–2494.
20 S.-H. Park, S. Lee, D. Moreira, P. R. Bandaru, I. Han and D.-J. Yun, *Sci. Rep.*, 2015, **5**, 15430.
21 B. Moser, K. Wasmer, L. Barbieri and J. Michler, *J. Mater. Res.*, 2007, **22**, 1004–1011.
22 F. Östlund, K. Rzepiejewska-Malyska, K. Leifer, L. M. Hale, Y. Tang, R. Ballarini, W. W. Gerberich and J. Michler, *Adv. Funct. Mater.*, 2009, **19**, 2439–2444.

23 S. Korte, J. S. Barnard, R. J. Stearn and W. J. Clegg, *Int. J. Plast.*, 2011, **27**, 1853–1866.
24 A. Montagne, S. Pathak, X. Maeder and J. Michler, *Ceram. Int.*, 2014, **40**, 2083–2090.
25 M. Chen, J. Wehrs, A. S. Sologubenko, J. Rabier, J. Michler and J. M. Wheeler, *Mater. Des.*, 2020, **189**, 108506.
26 M. Chen, L. Pethö, A. S. Sologubenko, H. Ma, J. Michler, R. Spolenak and J. M. Wheeler, *Nat. Commun.*, 2020, **11**, 2681.
27 S. Yan, Z. Xie and Q.-H. Qin, *J. Alloys Compd.*, 2025, **1010**, 177183.
28 B. Li, M. K. Kang, K. Lu, R. Huang, P. S. Ho, R. A. Allen and M. W. Cresswell, *Nano Lett.*, 2008, **8**, 92–98.
29 B. Li, Q. Zhao, H. Huang, Z. Luo, M. K. Kang, J.-H. Im, R. A. Allen, M. W. Cresswell, R. Huang and P. S. Ho, *J. Appl. Phys.*, 2009, **105**, 073510.
30 L. R. Meza, S. Das and J. R. Greer, *Science*, 2014, **345**, 1322–1326.
31 X. Zheng, H. Lee, T. H. Weisgraber, M. Shusteff, J. DeOtte, E. B. Duoss, J. D. Kuntz, M. M. Biener, Q. Ge, J. A. Jackson, S. O. Kucheyev, N. X. Fang and C. M. Spadaccini, *Science*, 2014, **344**, 1373–1377.
32 L. R. Meza, A. J. Zelhofer, N. Clarke, A. J. Mateos, D. M. Kochmann and J. R. Greer, *Proc. Natl. Acad. Sci. U. S. A.*, 2015, **112**, 11502–11507.
33 N. G. Dou, R. A. Jagt, C. M. Portela, J. R. Greer and A. J. Minnich, *Nano Lett.*, 2018, **18**, 4755–4761.
34 V. S. Deshpande, N. A. Fleck and M. F. Ashby, *J. Mech. Phys. Solids*, 2001, **49**, 1747–1769.
35 V. Pishchik, L. A. Lytvynov and E. R. Dobrovinskaya, *Sapphire: Material, Manufacturing, Applications*, Springer US, Boston, MA, 2009.
36 Y.-A. Chen, K.-C. Chien, I.-T. Chen and C.-H. Chang, *Micro Nano Eng.*, 2022, **14**, 100115.
37 G. Lin and Y. Huang, *Cryst. Res. Technol.*, 2018, **53**, 1800049.
38 C. Ji, Z. Zhang, K. D. Omotosho, D. Berman, B. Lee, R. Divan, S. Guha and E. V. Shevchenko, *ACS Nano*, 2022, **16**, 14754–14764.
39 K. Zhu, C. Wen, A. A. Aljarb, F. Xue, X. Xu, V. Tung, X. Zhang, H. N. Alshareef and M. Lanza, *Nat. Electron.*, 2021, **4**, 775–785.
40 V. R. Almeida, C. A. Barrios, R. R. Panepucci and M. Lipson, *Nature*, 2004, **431**, 1081–1084.
41 S. Y. Siew, B. Li, F. Gao, H. Y. Zheng, W. Zhang, P. Guo, S. W. Xie, A. Song, B. Dong, L. W. Luo, C. Li, X. Luo and G.-Q. Lo, *J. Lightwave Technol.*, 2021, **39**, 4374–4389.
42 M. L. Brongersma, Y. Cui and S. Fan, *Nat. Mater.*, 2014, **13**, 451–460.
43 K.-C. Chien, N. Graff, D. Djurdjanovic and C.-H. Chang, *J. Vac. Sci. Technol., B:Nanotechnol. Microelectron.:Mater., Process., Meas., Phenom.*, 2023, **41**, 062807.
44 K.-C. Chien and C.-H. Chang, *J. Vac. Sci. Technol., B: Nanotechnol. Microelectron.:Mater., Process., Meas., Phenom.*, 2022, **40**, 062802.
45 H. Chen, Q. Zhang and S. Y. Chou, *Nanotechnology*, 2015, **26**, 085302.
46 Y.-A. Chen, I.-T. Chen and C.-H. Chang, *J. Vac. Sci. Technol., B*, 2019, **37**, 061606.
47 W. C. Oliver and G. M. Pharr, *J. Mater. Res.*, 1992, **7**, 1564–1583.
48 W. G. Mao, Y. G. Shen and C. Lu, *J. Eur. Ceram. Soc.*, 2011, **31**, 1865–1871.
49 T. Y. Tsui and G. M. Pharr, *J. Mater. Res.*, 1999, **14**, 292–301.
50 M. F. Doerner, D. S. Gardner and W. D. Nix, *J. Mater. Res.*, 1986, **1**, 845–851.
51 M. A. Hopcroft, W. D. Nix and T. W. Kenny, *J. Microelectromech. Syst.*, 2010, **19**, 229–238.
52 E. Leonhard, *Methodus inveniendi lineas curvas maximi minimive proprietate gaudentes*, Marcum-Michaelem Bousquet, Lausanne & Geneva, 1744.
53 P. Sun, C. Jiang, Y. Jiang, D. Liu, L. Sun, S. Dun, Y. Li, Y. Ji and H. Liu, *Infrared Phys. Technol.*, 2024, **137**, 105184.
54 Y. Zhu, Q. Qin, F. Xu, F. Fan, Y. Ding, T. Zhang, B. J. Wiley and Z. L. Wang, *Phys. Rev. B:Condens. Matter Mater. Phys.*, 2012, **85**, 045443.
55 I.-T. Chen, F. R. Poblete, A. Bagal, Y. Zhu and C.-H. Chang, *Proc. Natl. Acad. Sci. U. S. A.*, 2022, **119**, e2201589119.